JOURNAL OF COMPUTATIONAL PHYSICS **123,** 296–310 (1996)
ARTICLE NO. 0025

A Dynamic Mesh Algorithm for Curvature Dependent Evolving Interfaces*

R. H. NOCHETTO

Department of Mathematics and Institute for Physical Science and Technology, University of Maryland, College Park, Maryland 20742

M. PAOLINI

Dipartimento di Matematica, Università di Milano, 20133 Milano, and Istituto di Analisi Numerica del CNR, 27100 Pavia, Italy

AND

C. VERDI

Dipartimento di Matematica, Università di Milano, 20133 Milano, Italy

Received July 13, 1994; revised June 5, 1995

A new finite element method is discussed for approximating evolving interfaces in $\mathbb{R}^n$ whose normal velocity equals mean curvature plus a forcing function. The method is insensitive to singularity formation and retains the local structure of the limit problem and, thus, exhibits a computational complexity typical of $\mathbb{R}^{n-1}$ without having the drawbacks of front-tracking strategies. A graded dynamic mesh around the propagating front is the sole partition present at any time step and is significantly smaller than a full mesh. Time stepping is explicit, but stability constraints force small time steps only when singularities develop, whereas relatively large time steps are allowed before or past singularities, when the evolution is smooth. The explicit marching scheme also guarantees that at most one layer of elements has to be added or deleted per time step, thereby making mesh updating simple and, thus, practical. Performance and potentials are fully documented via a number of numerical simulations in 2D, 3D, 4D, and 8D, with axial symmetries. They include tori and cones for the mean curvature flow, minimal and prescribed mean curvature surfaces with given boundary, fattening for smooth driving force, and volume constraint.

1. REACTION-DIFFUSION APPROACH WITH DOUBLE OBSTACLE

The ever increasing interest in the curvature dependent motion of fronts stems from its intrinsic mathematical beauty and difficulty, as well as its applications to phase transitions in materials science, flame propagation, combustion theory, crystal growth, etc. [13]. In its classical formulation, let $\Sigma(t) \subset \mathbb{R}^n$ be an oriented interface which splits $\mathbb{R}^n$ into two disjoint regions, the inside $I(t)$ and outside $O(t)$ of $\Sigma(t)$, and let $\mathbf{n}$ be the unit normal vector to $\Sigma(t)$ pointing towards $I(t)$. The surface $\Sigma(t)$ propagates in the normal direction $\mathbf{n}$ with velocity

$$V = \kappa + g, \tag{1.1}$$

where κ stands for the sum of the principal curvatures (positive if $I(t)$ is locally mean convex) and $g = g(\mathbf{x}, t)$ is a forcing function. The evolution of $\Sigma(t)$ may exhibit singularities and topological changes, such as breaking, merging and extinction. So the classical geometric approach fails to describe the problem past singularities, and *front-tracking* methods (FT) may also break down [16]. They do not only have to compute κ explicitly, a delicate issue for large principal curvatures but small κ, but also rely on a catalog of singularities to replace (1.1) whenever breaking or merging occurs. It is not surprising then that FT are not proven to converge as the discretization parameters tend to zero, most notably for unsmooth flows. When applicable in 2D, however, FT are efficient due to their low computational complexity.

We present a *dynamic mesh algorithm* (DMA) insensitive to singularity formation which retains the local structure of the geometric flow, and thus the computational complexity typical of $\mathbb{R}^{n-1}$. Our method extends naturally to higher dimensions, requiring mainly an efficient mesh generator, whereas implementing FT for tracking interfaces in higher dimensions is a nontrivial matter. Preliminary results were reported in [20], and the theoretical foundations in [21–26, 29]. It is based on combining a singularly perturbed reaction-diffusion equation, the so-called Allen–Cahn equation, with a double obstacle potential.

* Partially supported by NSF Grant DMS-9305935, MURST, and CNR Contract 94.00139.01.

0021-9991/96 $18.00

Given a small relaxation parameter $\varepsilon > 0$ and a density function $0 < a^* \le a = a(\mathbf{x}) \le A$, the nonlinear PDE reads formally

$$\varepsilon \partial_t (a\chi_\varepsilon) - \varepsilon \operatorname{div}(a \nabla \chi_\varepsilon) + \frac{1}{2a\varepsilon} \Psi'(\chi_\varepsilon) = \frac{c_0}{2} g \quad \text{in } \Omega \times (0, \infty) \tag{1.2}$$

and is subject to initial and boundary conditions

$$\chi_\varepsilon(\cdot, 0) = \chi_\varepsilon^0(\cdot) \quad \text{in } \Omega, \quad \chi_\varepsilon = f \quad \text{on } \partial\Omega \times (0, \infty).$$

The inequality in (1.2) must be interpreted in the sense of graphs. The zero level set $\Sigma_\varepsilon(t)$ of $\chi_\varepsilon(\cdot, t)$ is regarded as an approximation of $\Sigma(t)$. Hereafter Ψ stands for the following double obstacle potential with wells of equal depth located at ± 1,

$$\Psi(s) := \begin{cases} 1 - s^2 & \text{if } s \in [-1, 1] \\ +\infty & \text{if } s \notin [-1, 1], \end{cases} \tag{1.3}$$

$c_0 := \int_{-1}^{1} \Psi^{1/2}(s)\, ds = \pi/2$ is a scaling factor, and Ω is a bounded domain in $\mathbb{R}^n$ with $n \ge 2$. The zero level set of χ_ε^0 coincides with $\Sigma^0 = \Sigma(0)$ and $\chi_\varepsilon^0 < 0$ in $I(0)$, and its shape is extremely important to avoid an initial transient and is discussed in Section 2, along with the choice of f to simulate the various flows of interest. We may think of $f = 1$ for the moment.

Because of the double obstacle ∓ 1, χ_ε is thus forced to satisfy $|\chi_\varepsilon| \le 1$ irrespective of g, but more importantly $\chi_\varepsilon(\cdot, t)$ attains the values -1 or $+1$ outside a narrow transition layer $\mathscr{T}_\varepsilon(t)$ of local size $\mathscr{O}(\varepsilon a(\mathbf{x}))$ in the vicinity of any regular point $x \in \Sigma(t)$ [23]. The product $\varepsilon a(\mathbf{x})$ is thus the effective relaxation parameter, which is space dependent and graded towards singularities where it attains its minimum εa^*. Since $a(\mathbf{x})$ is given, we presume that singularity location is independent of time and known in advance. Even though this is indeed the case in our simulations of Section 5, an adaptive design of a space-time dependent $a(\mathbf{x}, t)$ would be necessary in general.

The crucial property $|\chi_\varepsilon(\cdot, t)| = 1$ outside $\mathscr{T}_\varepsilon(t)$ is here exploited numerically in that one only has to solve (1.2) within $\mathscr{T}_\varepsilon(t)$, which is a relatively small region. On the other hand our ability to control layer thickness results in enhanced pointwise accuracy because it can alleviate the smearing effect associated with singularities. For the alternative choice of potential $\Psi(s) = (1 - s^2)^2$, the boundary values of χ_ε must depend on g, and even for $g = 0$ they cannot be taken to be either -1 or $+1$. Any attempt to reduce the computation to a strip around $\Sigma_\varepsilon(t)$ has to deal with this very delicate issue, which is completely circumvented via (1.3).

DMA triangulates solely the transition region $\mathscr{T}_\varepsilon(t)$, and then updates the resulting mesh to follow the layer motion; see Section 4. This results in savings of both computing time and memory allocation. The underlying finite element mesh is locally refined according to the mesh density function $ha(\mathbf{x})$, with $h > 0$ being a global mesh parameter. Both h and ε are related so as to guarantee numerical resolution of $\mathscr{T}_\varepsilon(t)$ and the optimal distribution of spatial degrees of freedom. Forward differences are used in time with adaptive selection of time step τ depending on the smallest triangle size within $\mathscr{T}_\varepsilon(t)$, namely $\tau \le Ch^2 \min_{\mathbf{x} \in \mathscr{T}_\varepsilon(t)} a^2(\mathbf{x})$, because $\mathscr{T}_\varepsilon(t)$ is the active set for stability considerations. This would not be possible for a regular potential like $\Psi(s) = (1 - s^2)^2$, for which $\mathscr{T}_\varepsilon(t) = \Omega$. Since a is designed to be small only near singular points, relatively large time steps are allowed at the beginning or past singularities, when the evolution is smooth. The explicit nature of the scheme exhibits two further advantages. First, it guarantees that at most one layer of elements has to be added or deleted per time step (finite speed of propagation), thereby making mesh updating simple and, thus, practical. Second, its coupling with appropriate numerical quadrature (mass lumping) yields a trivial algebraic problem that reduces to a matrix–vector product followed by a componentwise truncation to meet the obstacle constraint. Consequently there is no iteration involved.

The limit of $\Sigma_\varepsilon(t)$ as $\varepsilon \downarrow 0$ gives a notion of generalized evolution $\Sigma(t)$ that was reconciled in [19], for regular potentials Ψ and $a = 1$, with the varifold approach which, in turn, may lack uniqueness past singularities [10]. The latter is reflected in high sensitivity of (1.2) to initial data and will be illustrated with a couple of examples in Section 5.2 (see also Remark 2.2). The *level set approach* (LS), on the other hand, provides a unique notion of generalized evolution by letting evolve all the level sets of an unknown function ω according to (1.1), which in terms of ω reads [27, 31]

$$\frac{\partial_t \omega}{|\nabla \omega|} = \operatorname{div}\left(\frac{\nabla \omega}{|\nabla \omega|}\right) + g \quad \text{in } \mathbb{R}^n \times (0, \infty), \qquad \omega(\cdot, 0) = \omega^0(\cdot) \quad \text{in } \mathbb{R}^n. \tag{1.4}$$

This is a degenerate nonlinear parabolic PDE that must be interpreted in the viscosity sense [14, 18]. The sign of ω^0 coincides with that of χ_ε^0 outside Σ^0. The generalized evolution $\Sigma(t)$ is defined to be the zero level set of $\omega(\cdot, t)$ and coincides with the limit of $\Sigma_\varepsilon(t)$ in case of no fattening [3, 11, 17], again for regular potentials. A convergence theory for the singular potential (1.3) has been developed [21–24], which extends to an implicit fully discrete approximation [25] as well as an explicit time-stepping with quad-

rature [26]. The effect of variable relaxation parameter and graded meshes is still an open problem. In contrast no convergence results are known for any full discretization of (1.4).

Our method compares favorably with the implicit scheme of [8] which exploits (1.3) as well, but works over a quasi-uniform partition of Ω with $a = 1$; see Section 5.1.1. Explicit time stepping is also advantageous with respect to LS implemented over uniform partitions of Ω in that the stability constraint is then dictated by the smallest meshsize through the whole calculation [27, 31]. Moreover, LS is global and so effectively increases the problem dimension by one. This is not an issue for our method, that retains dimensionality and so the computational complexity typical of $\mathbb{R}^{n-1}$.

We present a number of numerical simulations in Section 5. We start with the circle in 2D as a benchmark calculation. We show notorious gains in computing time for a desired accuracy with respect to both a global graded mesh or a uniform dynamic mesh. We continue with tori in 3D and 4D with axial symmetry; new singularities seems to emerge from these simulations. Our emphasis is placed on the calculation of critical parameters which lead to the blowup of principal curvatures whereas their sum κ may remain comparatively small. These cases are critical for FT. By enforcing suitable Dirichlet boundary conditions we can examine cones in 2D, 4D, and 8D and, also, find minimal surfaces and surfaces of prescribed mean curvature with given boundary as the asymptotic limit of (1.2) for $t \to \infty$. This provides a rigorous justification to the cutting strategy of [6]. We illustrate how to detect fattening via two examples with smooth forcing g. We conclude with volume preserving mean curvature flows cast as a nonlocal (1.2) with a multiplier [8, 12, 30]. These examples cannot be solved with LS and make the implementation of FT delicate because of the nonlocal (volume) constraint.

The rest of the paper is organized as follows. In Section 2 we formulate the double obstacle problem in axial symmetry. The fully discrete scheme is tackled in Section 3, whereas implementation issues for the dynamic mesh algorithm are discussed in Section 4. Flexibility and potentials of the proposed method are fully documented in Section 5 with several numerical experiments. A summary of crucial properties of DMA concludes the paper in Section 6.

2. VARIATIONAL FORMULATION IN AXIAL SYMMETRY

We intend to reformulate (1.2) as a variational inequality in an axially symmetric domain Ω. Upon splitting $\mathbb{R}^n = \mathbb{R}^{n_1} \times \mathbb{R}^{n_2}$, we denote any point in $\mathbb{R}^n$ by $(\mathbf{x}_1, \mathbf{x}_2)$ with $\mathbf{x}_1 \in \mathbb{R}^{n_1}$, $\mathbf{x}_2 \in \mathbb{R}^{n_2}$. We set $\mathbf{z} = (z_1, z_2)$, where z_i indicates either $|\mathbf{x}_i|$ if $n_1 \geq 1$ or x_i (no reflection around the $x_i = 0$ axis) if $n_i = 1$. We also set

$$Z = \{\mathbf{z} \in \mathbb{R}^2 : (\mathbf{x}_1, \mathbf{x}_2) \in \Omega\},$$
$$\partial_e Z = \partial Z \backslash \{\mathbf{z} : z_i = |\mathbf{x}_i| = 0, i = 1 \text{ or } 2\}.$$

We assume that ω^0, χ^0_ε, g, a, f are axially symmetric; that is, they just depend on z_1, z_2; then so are $\omega(\cdot, t)$, $\chi_\varepsilon(\cdot, t)$ for $t > 0$. To simplify notation, we keep the same symbols for all functions ω^0, ω, χ^0_ε, χ_ε, a, g, f and sets Σ^0, $\Sigma(t)$, $\Sigma_\varepsilon(t)$ involved, even though they now depend only on the variable $\mathbf{z} \in Z$. The initial front $\Sigma^0 \subset Z$ has bounded curvature. The density function $a = a(\mathbf{z})$ satisfies $a \in W^1_\infty(Z)$.

Letting γ be the standing wave for (1.2),

$$\gamma(x) = -1 \quad \text{if } x < -\frac{\pi}{2}, \quad \gamma(x) = \sin x \quad \text{if } x \in \left[-\frac{\pi}{2}, \frac{\pi}{2}\right],$$
$$\gamma(x) = +1 \quad \text{if } x > \frac{\pi}{2},$$

the initial datum for (1.2) is defined in terms of the signed distance function d^0 to Σ^0 by

$$\chi^0_\varepsilon(\mathbf{z}) = \gamma\left(\frac{d^0(\mathbf{z})}{\varepsilon\, a((\mathbf{z} + s(\mathbf{z}))/2)}\right) \quad \forall \mathbf{z} \in Z, \tag{2.1}$$

where $\mathbf{s}(\mathbf{z}) \in \Sigma^0$ is the projection of $\mathbf{z}$ onto Σ^0. Note that $\Sigma_\varepsilon(0) = \Sigma^0$ and χ^0_ε approximates the first two terms of the inner asymptotic expansion of χ_ε [22, 29] which, in turn, alleviates the initial transient regime. If $\Sigma(t) \subset \Omega$ for all t, then the boundary datum f for (1.2) is $f = 1$. Instead, in order to simulate flows intersecting the boundary at Γ, that is, $\Sigma(t) \cap \partial\Omega = \Gamma \neq \emptyset$, then $f = \chi^0_\varepsilon$ on $\partial\Omega$.

We indicate with L^2_ζ and H^1_ζ the usual energy spaces with weight $\zeta(\mathbf{z}) = z_1^{n_1-1} z_2^{n_2-1}$, and introduce the convex set

$$\mathcal{K}_\zeta = \{\varphi \in H^1_\zeta(Z) : |\varphi| \leq 1 \text{ in } Z,\ \varphi = f \text{ on } \partial_e Z\}.$$

Let $\omega_k = (k+1)\,(\pi^{(k+1)/2}/\Gamma((3+k)/2))$ be the surface measure of the k-sphere S^k but let $\omega_{n_i-1} = 1$ (instead of 2) if $n_i = 1$ and $z_i = x_i$ (no reflection around the $x_i = 0$ axis). Then note that

$$\int_\Omega \varphi(z_1, z_2)\, d\mathbf{x}_1\, d\mathbf{x}_2 = \omega_{n_1-1}\omega_{n_2-1} \int_Z \varphi(\mathbf{z})\zeta(\mathbf{z})\, d\mathbf{z},$$
$$\nabla\varphi \cdot \nabla\phi = \nabla_{\mathbf{z}}\varphi \cdot \nabla_{\mathbf{z}}\phi.$$

The 2D variational inequality equivalent to (1.2) then

reads: *find* $\chi_\varepsilon \in L^2(0,\infty;\mathscr{K}_\zeta)\cap H^1(0,\infty;L^2_\zeta(Z))$ *such that* $\chi_\varepsilon(\cdot,0)=\chi^0_\varepsilon(\cdot)$ *and, for a.e.* $t\in(0,\infty)$ *and all* $\varphi\in\mathscr{K}_\zeta$,

$$\int_Z\Big(\varepsilon\partial_t(a\chi_\varepsilon)(\varphi-\chi_\varepsilon)+\varepsilon a\,\nabla_{\mathbf{z}}\chi_\varepsilon\cdot\nabla_{\mathbf{z}}(\varphi-\chi_\varepsilon) - \frac{1}{\varepsilon a}\chi_\varepsilon(\varphi-\chi_\varepsilon)-\frac{\pi}{4}g(\varphi-\chi_\varepsilon)\Big)\zeta\,d\mathbf{z}\ge 0. \tag{2.2}$$

Remark 2.1 (Classical approach). The sum of the principal curvatures κ becomes

$$\kappa=\hat\kappa-(n_1-1)\frac{\nu_1}{z_1}-(n_2-1)\frac{\nu_2}{z_2} \tag{2.3}$$

in axial symmetry, where $\hat\kappa$ and ν stand for the usual curvature and inner normal vector in 2D. Most of our simulations of Section 5 investigate *critical* singularities, which may correspond to κ smaller than the blowing-up principal curvatures. This cancellation is a higher dimensional effect, even with axial symmetry in $\mathbb{R}^{n_1+n_2}$, and distinguishes the motion of a curve ($n_1+n_2=2$) from the evolution of an axially symmetric surface ($n_1+n_2>2$).

Remark 2.2 (Fattening). If $\Sigma^{\lambda_*}(t)=\{\mathbf{z}\in Z:\omega(\mathbf{z},t)=\lambda_*\}$ develops interior for some λ_*, we say that $\Sigma^{\lambda_*}(t)$ fattens up. Since this notion involves ω, viscosity solution to (1.4), the question arises as to how to characterize fattening in terms of χ^λ_ε, variational solution to (2.2) with initial datum centered around $\Sigma^\lambda(0)$. The volume $|A^\lambda(t)|$ of $A^\lambda(t)=\{\mathbf{x}\in\Omega:\omega(\mathbf{x},t)\le\lambda\}$ is clearly a nondecreasing function of λ. Since $\Sigma^{\lambda_*}(t)=(\bigcap_{\lambda>\lambda_*}A^\lambda(t))\backslash(\bigcup_{\lambda<\lambda_*}A^\lambda(t))$, it follows that

$$|\Sigma^{\lambda_*}(t)|=\lim_{\lambda\downarrow\lambda_*}|A^\lambda(t)|-\lim_{\lambda\uparrow\lambda_*}|A^\lambda(t)|=[\![|A^\lambda(t)|]\!]_{\lambda_*}; \tag{2.4}$$

that is, fattening of $\Sigma^{\lambda_*}(t_*)$ corresponds to a jump of $|A^\lambda(t)|$ at $\lambda=\lambda_*$, for any (fixed) t such that $0<t-t_*\ll 1$. We can thus approximate $A^\lambda(t)$ with $A^\lambda_\varepsilon=\{\mathbf{x}\in\Omega:\chi^\lambda_\varepsilon(\mathbf{x},t)\le 0\}$ in (2.4), and exploit high (exponential sensitivity of $|A^\lambda_\varepsilon|$ with respect to ε, to detect fattening (see Sections 5.2.1, 5.2.2). Since DMA evolves one level set at a time, as dictated by χ^0_ε, it avoids interaction between nearby level sets. Even though this property is also valid for (1.4), it is no longer true for a discrete counterpart of (1.4). We expect flat regions of ω to be replaced by regions with small slope depending on the discretization and regularization parameters. Estimation of $[\![|A^\lambda(t)|]\!]_{\lambda_*}$ would thus require an intricate tuning of λ and such parameters.

Remark 2.3 (Volume preserving mean curvature flow). This flow can be described in terms of (1.2) with a time dependent multiplier $\mu(t)$ in place of the forcing term g [8, 12, 30]. The variational inequality (2.2) is replaced by

$$\int_Z\Big(\varepsilon\partial_t(a\chi_\varepsilon)(\varphi-\chi_\varepsilon)+\varepsilon a\,\nabla_{\mathbf{z}}\chi\varepsilon\cdot\nabla_{\mathbf{z}}(\varphi-\chi_\varepsilon)-\frac{1}{\varepsilon a}\chi_\varepsilon(\varphi-\chi_\varepsilon)-\frac{\pi}{4}\mu(\varphi-\chi_\varepsilon)\Big)\zeta\,d\mathbf{z}\ge 0, \tag{2.5}$$

$$\int_Z\chi_\varepsilon\zeta\,d\mathbf{z}=\int_Z\chi^0_\varepsilon\zeta\,d\mathbf{z}. \tag{2.6}$$

Equation (1.1) is then substituted by the nonlocal law $V=\kappa-(1/|\Sigma(t)|)\int_{\Sigma(t)}\kappa$. Consequently, the steady state solution ($V=0$) corresponds to a surface $\Sigma(\infty)$ with constant mean curvature and can be computed as the asymptotic limit $t\to\infty$. The resulting flow $\Sigma(t)$ cannot be described via LS.

3. DYNAMIC MESH ALGORITHM: FORMULATION

Continuous piecewise linear finite elements are used for space discretization of (2.2) together with forward differences in time. Let mesh density $\mathscr{H}$ and relaxation parameter $\mathscr{E}$ be given by

$$\mathscr{H}(\mathbf{z})=ha(\mathbf{z}),\quad \mathscr{E}(\mathbf{z})=\varepsilon a(\mathbf{z})\quad\forall\,\mathbf{z}\in Z. \tag{3.1}$$

Let $\mathscr{P}$ be a partition of Z into triangles (elements) S of size h_S comparable with $\mathscr{H}(\mathbf{b}_S)$ and barycenter $\mathbf{b}_S$; for simplicity we assume $\overline{Z}=\bigcup_{S\in\mathscr{P}}S$. Elements satisfy the minimum angle condition (regularity of $\mathscr{P}$) and the geometric constraint that the sum of interior angles opposite to a common interelement side do not exceed π (weak acuteness) [15, 33]. The latter yields a global Delaunay triangulation $\mathscr{P}$, which is introduced here for convenience only but is never fully present. A rather small part of it is employed by our method at each time step; see Fig. 5.4.

If $\mathbb{P}^1(S)$ denotes the set of linear polynomials restricted to $S\in\mathscr{P}$, then the basic finite element space $\mathscr{V}^1_{\mathscr{P}}$ over $\mathscr{P}$ is

$$\mathscr{V}^1_{\mathscr{P}}=\{\varphi\in W^1_\infty(Z):\varphi_{|S}\in\mathbb{P}^1(S)\;\forall\,S\in\mathscr{P}\}.$$

Let $\{\mathbf{z}_j\}_{j=1}^J$ be the set of all nodes of $\mathscr{P}$ and $\{\varphi_j\}_{j=1}^J$ be the canonical basis functions of $\mathscr{V}^1_{\mathscr{P}}$, that is, $\varphi_l(\mathbf{z}_j)=\delta_{jl}$. Let $\Pi_S:C^0(S)\to\mathbb{P}^1(S)$ be the usual (local) Lagrange operator that interpolates at the vertices of S with a linear polynomial. Mass matrices $\mathbf{M}_k=\{m^k_{jl}\}_{jl}$ $(k=-1,0,1)$ and stiffness matrix $\mathbf{K}=\{k_{jl}\}_{jl}$ are given by

$$m^k_{jl}=\sum_{S\in\mathscr{P}}\int_S a^k(\mathbf{b}_S)\Pi_S(\varphi_j\varphi_l)\zeta\,d\mathbf{z},$$

$$k_{jl}=\sum_{S\in\mathscr{P}}\int_S a(\mathbf{b}_S)\,\nabla\varphi_j\cdot\nabla\varphi_l\,\zeta\,d\mathbf{z},$$

where a^k stands for either $1/a$, 1, or a as $k = -1, 0, 1$. Each element contribution can be evaluated easily using suitable quadrature rules and then assembled [15, 33]. The replacement of $\varphi_j\varphi_l$ by $\Pi_S(\varphi_j\varphi_l)$ in m_{jl}^k is the so-called vertex quadrature rule and has the effect of diagonalizing the resulting matrix (mass lumping); in fact, $m_{jl}^k = 0$ if $j \neq l$. The discrete convex set over $\mathscr{P}$ is defined by

$$\mathscr{K}_{\mathscr{P}} = \{\varphi \in \mathscr{V}_{\mathscr{P}}^1 : |\varphi(\mathbf{z})| \leq 1 \ \forall\, \mathbf{z} \in Z,$$
$$\varphi(\mathbf{z}_j) = f(\mathbf{z}_j) \ \forall\, \mathbf{z}_j \in \partial_e Z\}.$$

To motivate the actual algorithm, we examine the solution $X^{i+1} \in \mathscr{V}_{\mathscr{P}}^1$ to the following full discretization of (2.2), which uses C^0 piecewise linear elements in space and forward differences in time,

$$\begin{aligned}\sum_{S\in\mathscr{P}} \int_S \Bigg(& \varepsilon a(\mathbf{b}_S)\Pi_S((X^{i+1} - X^i)(\varphi - X^{i+1})) \\ & + \tau^i \varepsilon a(\mathbf{b}_S)\nabla X^i \cdot \nabla(\varphi - X^{i+1}) \\ & - \frac{\tau^i}{\varepsilon a(\mathbf{b}_S)} \Pi_S(X^i(\varphi - X^{i+1})) \\ & - \tau^i \frac{\pi}{4} \Pi_S(g^{i+1}(\varphi - X^{i+1}))\Bigg)\, \zeta\, d\mathbf{z} \geq 0\end{aligned} \tag{3.2}$$

for all $\varphi \in \mathscr{K}_{\mathscr{P}}$. It is instructive to write (3.2) into matrix form. To this end, let $\mathbf{P} : \mathbb{R}^J \to \mathbb{R}^J$ be the componentwise projection on $[-1, 1]$ defined by $(\mathbf{Pq})_j = \max(-1, \min(1, q_j))$ for $\mathbf{q} = \{q_j\}_{j=1}^J$. If we identify any function of $\mathscr{V}_{\mathscr{P}}^1$ with the vector of $\mathbb{R}^J$ of its nodal values and set $g^{i+1} = \{g^{i+1}(\mathbf{z}_j)\}$, then (3.2) can be written equivalently as a *two-step* process:

$$\begin{aligned} X^{i+1/2} &= (\mathbf{M}_1)^{-1}\left(\left(\mathbf{M}_1 - \tau^i\mathbf{K} + \frac{\tau^i}{\varepsilon^2}\mathbf{M}_{-1}\right)X^i \right.\\ &\qquad \left. + \frac{\delta^i}{\varepsilon}\,\frac{\pi}{4}\mathbf{M}_0 g^{i+1}\right), \\ X^{i+1} &= \mathbf{P}X^{i+1/2}.\end{aligned} \tag{3.3}$$

The actual computation of X^{i+1} is thus trivial in that we first have to perform the matrix–vector products involved on the right-hand side of (3.3) to define $X^{i+1/2}$ (updating), and then project each component of $X^{i+1/2}$ onto $[-1, 1]$ to compute X^{i+1} (truncation). We stress that no iteration is involved.

If $\mathbf{z}_j$ is a node of $\mathscr{P}$ such that $X_l^i = X^i(\mathbf{z}_l) = 1$ (resp. -1) for all adjacent nodes $\mathbf{z}_l$ to $\mathbf{z}_j$, including $\mathbf{z}_j$, then (3.3) reduces to

$$\begin{aligned} X_j^{i+1/2} = X_j^i\left(1 + \frac{\tau^i}{\varepsilon^2}\,\frac{m_{jj}^{-1}}{m_{jj}^1}\right) + \frac{\delta^i}{\varepsilon}\,\frac{\pi}{4}\,\frac{m_{jj}^0}{m_{jj}^1} g_j^{i+1} > X_j^i = 1 \\ (\text{resp. } < X_j^i = -1)\end{aligned} \tag{3.4}$$

for ε so small that $|g| \leq 4/A\varepsilon\pi$. Therefore $X_j^{i+1} = X_j^i = 1$ (resp. -1), which says that the discrete transition layer (noncoincidence set),

$$T^i = \cup\{S \in \mathscr{P} : |X^i(\mathbf{b}_S)| < 1\},$$

cannot move faster than one triangle per time step (*finite speed of propagation*) and, consequently, X^{i+1} does not have to be computed at vertices lying outside T^i.

With this crucial property at hand, we realize that there is no need for the entire partition $\mathscr{P}$ but just for a rather small part of it. We thus introduce the *dynamic* mesh $\mathscr{D}^i$, and enlarged transition layer (or active domain) D^i,

$$\mathscr{D}^i = \{S \in \mathscr{P} : S \cap T^i \neq \emptyset\}, \quad D^i = \cup_{S\in\mathscr{D}^i} S.$$

We point out that $\mathscr{D}^i$ consists of all elements without T^i and a layer of boundary (or security) triangles and is the sole decomposition of Z present. The label dynamic reflects the fact that $\mathscr{D}^i$ has to be updated every time step to incorporate or delete security elements for the new transition region T^{i+1}; this procedure is further discussed in Section 4.

We consider the following variant of (3.2) called *dynamic mesh algorithm* (DMA). We *construct* $\mathscr{D}^0$ *and set* $X^0 = \sum_{j=1}^{J^0} \chi_\varepsilon^0(\mathbf{z}_j)\varphi_j \in \mathscr{K}_{\mathscr{D}^0}$ *and* $\Sigma^0 = \{\mathbf{z} \in D^0 : X^0(\mathbf{z}) = 0\}$. We then *suppose that* $\mathscr{D}^i$ *and the iterate* $X^i \in \mathscr{K}_{\mathscr{D}^i}$ *has been already found along with* Σ^i *for* $i \geq 0$. We denote by $\mathbf{M}_k^i$ and $\mathbf{K}^i$ the mass and stiffness submatrices corresponding to the J^i nodes of $\mathscr{D}^i$. We *execute the following four steps to compute* X^{i+1}, Σ^{i+1}, *and* $\mathscr{D}^{i+1}$:

Step 1. the time-step τ^i is chosen adaptively to meet the stability test within $\mathscr{D}^i$,

$$0 < \sigma \leq \tau^i \|(\mathbf{M}_1^i)^{-1}\mathbf{K}^i\|_\infty < 1; \tag{3.5}$$

Step 2. the iterate $X^{i+1} \in \mathscr{K}_{\mathscr{D}^i}$ is determined as the unique solution to (3.3) within D^i,

$$\begin{aligned} X^{i+1/2} &= (\mathbf{M}_1^i)^{-1}\left(\left(\mathbf{M}_1^i - \tau^i\mathbf{K}^i + \frac{\tau^i}{\varepsilon^2}\mathbf{M}_{-1}^i\right)X^i \right.\\ &\qquad \left. + \frac{\delta^i}{\varepsilon}\,\frac{\pi}{4}\,\mathbf{M}_0^i\, g^{i+1}\right), \\ X^{i+1} &= \mathbf{P}X^{i+1/2};\end{aligned} \tag{3.6}$$

Step 3. the discrete interface Σ^{i+1} is computed according to

$$\Sigma^{i+1} = \{\mathbf{z} \in D^i : X^{i+1}(\mathbf{z}) = 0\};$$

Step 4. the dynamic mesh $\mathscr{D}^i$ is updated by adding security triangles that intersect T^{i+1} or deleting ones whose intersection with T^{i+1} is empty; $\mathscr{D}^{i+1}$ is thus created.

Remark 3.1 (Stability). Condition (3.5) is achieved by an automatic reduction or increase of τ^{i-1} by the factors σ or $1/\sigma$ and is tailored to avoid oscillations: a node value of X^i cannot jump from 1 to -1 even if all the adjacent values are -1. It implies the usual stability constraint for explicit methods,

$$\tau^i \le Ch^2 \min_{\mathbf{z}\in D^i} a^2(\mathbf{z}), \tag{3.7}$$

where C depends on mesh regularity but not on i. Since (3.7) has to be met only in the active region D^i, which is significantly smaller than Z and a is small near singularities only, we realize that relatively large time steps can be used when the evolution is smooth even past singularities. This is advantageous with respect to more standard explicit discretizations which suffer from (3.7) through the entire calculation [1, 27, 31].

Remark 3.2 (Layer resolution). The measure $d\mu(t) = (\varepsilon a|\nabla\chi_\varepsilon|^2 + \Psi(\chi_\varepsilon)/\varepsilon a\, dx$ is known to converge weakly to the surface measure over $\Sigma(t)$, at least provided $a = 1$ and Ψ is smooth [19]. This assertion results from Γ-convergence for steady state problems and their discrete counterparts, even with double obstacles [5, 29]. Since the mass of $d\mu(t)$ is concentrated in $\mathscr{T}_\varepsilon(t)$, we then infer that $\mathscr{T}_\varepsilon(t)$ must be resolved to capture the correct asymptotic limit. In view of (3.1) and the fact that the local thickness of T^i is approximately $\pi\varepsilon a(\mathbf{z})$, the relation $h = \mathscr{O}(\varepsilon)$ is enforced in practice; note that this supersedes asymptotically the absolute stability bound $h \le \pi\varepsilon/2$. The number of triangles in the transversal direction is $\approx \pi a(\mathbf{z})\varepsilon/a(\mathbf{z})h = 1/\mathscr{O}(1)$ for any $\mathbf{z} \in T^i$, which is taken to be between 10 and 20 for practical purposes. Since $\mathscr{D}^i$ is thus minimal in terms of number of triangles, the computational complexity of our method is comparable with that of FT but much better than that of LS [1, 27, 31].

Remark 3.3 (Velocity bound). The fact that the discrete transition layer moves one element at most entails the bound $V_S \le h_S/\tau^i$ for the discrete front velocity of any $S \in \mathscr{D}^i$. If $S \in \mathscr{D}^i$ is the smallest triangle, then $\tau^i \approx Ch_S^2$ and so V_S satisfies

$$V_S \le \frac{h_S}{\tau^i} \approx \frac{C}{h_S} \le \frac{C}{ha^*}. \tag{3.8}$$

In view of (1.1) and g being bounded, we realize that (3.8) dictates scheme resolution because curvatures beyond $\mathscr{O}(1/ha^*)$ will not be resolved. The improvement gained via a variable relaxation $\mathscr{E}$ is again evident.

Remark 3.4 (Implicit scheme). It is customary for parabolic problems to use implicit time stepping. We stress that the choice of an explicit scheme may not be restrictive in this setting. An implicit scheme would require $\tau^i \le C(\varepsilon a)^2$ in D^i just for solvability of (3.2) which, together with the relation $h = \mathscr{O}(\varepsilon)$ necessary for transition layer resolution [5], would anyhow imply $\tau^i \le Ch_S^2$ for a basically linear relation between h and ε. In addition, T^i may move further than one element, thereby making mesh updating difficult or impractical.

Remark 3.5. (Exact integration). Crucial remark (3.4) is still valid without mass lumping, that is, with Π_S in (3.2) replaced by the identity. Consider $a = 1$, for simplicity, and let $X_l^i = 1$ for all adjacent nodes $\mathbf{z}_l$ to $\mathbf{z}_j$, including $\mathbf{z}_j$, and suppose $X_j^{i+1} < 1$. Since

$$\int_Z X^{i+1}\varphi_j\zeta\, d\mathbf{z} \ge \int_Z \left(\left(1 + \frac{\tau^i}{\varepsilon^2}\right) X^i\varphi_j - \tau^i \nabla X^i\cdot\nabla\varphi_j + \frac{\delta^i}{\varepsilon}\frac{\pi}{4} g^{i+1}\varphi_j\right)\zeta\, d\mathbf{z},$$

as results from (3.2) with exact integration and $\varphi = X^{i+1} + (1 - X_j^{i+1})\varphi_j$, we make use of $X^{i+1} \le 1$ to arrive at

$$\int_Z \varphi_j\zeta\, d\mathbf{z} > \int_Z X^{i+1}\varphi_j\zeta\, d\mathbf{z} \ge \int_Z \left(1 + \frac{\tau^i}{\varepsilon^2} + \frac{\delta^i}{\varepsilon}\frac{\pi}{4} g^{i+1}\right)\varphi_j\zeta\, d\mathbf{z} \ge \int_Z \varphi_j\zeta\, d\mathbf{z},$$

which is a contradiction. Therefore mass lumping is not justified in light of (3.4) but rather in terms of solvability. In fact $\mathbf{M}_1^i$ would no longer be diagonal and thus an iterative procedure would be needed to compute X^{i+1} in (3.6).

Remark 3.6 (Volume constraint). The discrete version of (2.5) and (2.6) reads: *construct* $\mathscr{D}^0$ *and set* $X^0 = \sum_{j=1}^{J^0} \chi_\varepsilon^0(\mathbf{z}_j)\varphi_j \in \mathscr{K}_{\mathscr{D}^0}$, $\Sigma^0 = \{\mathbf{z} \in D^0 : X^0(\mathbf{z}) = 0\}$, *and* $m = \int_Z X^0\zeta\, d\mathbf{z}$; *if* $\mathscr{D}^i$ *and* X^i *are already known for* $i \ge 0$, *let* τ^i *be the time step satisfying* (3.5) *and find* $X^{i+1} \in \mathscr{K}_{\mathscr{D}^i}$, $\mu^{i+1} \in \mathbb{R}$, *according to*

$$X^{i+1/2} = (\mathbf{M}_1^i)^{-1}\left(\left(\mathbf{M}_1^i - \tau^i\mathbf{K}^i + \frac{\tau^i}{\varepsilon^2}\mathbf{M}_{-1}^i\right)X^i + \frac{\delta^i}{\varepsilon}\frac{\pi}{4}\mathbf{M}_0^i\mu^{i+1}\right),$$

$$X^{i+1} = \mathbf{P}X^{i+1/2}, \tag{3.9}$$

$$\int_Z X^{i+1}\zeta\, d\mathbf{z} = m, \tag{3.10}$$

Σ^{i+1} *as in* Step 3 *and finally* $\mathscr{D}^{i+1}$ *as in* Step 4. Solution of

(3.9) for a given μ is denoted $X^{i+1}(\mu)$. Since function $F^{i+1}(\mu) = \int_Z X^{i+1}(\mu)\,\zeta\,d\mathbf{z} - m$ is continuous and strictly increasing, and $\lim_{\mu\to\pm\infty} F^{i+1}(\mu) = \pm|\Omega| - m \gtrless 0$, problem (3.9), (3.10) admits a unique solution $\{X^{i+1}, \mu^{i+1}\}$.

The stability test on the multiplier for (3.4) to hold, namely $|\mu^{i+1}| \le 4/A\varepsilon\pi$, dictates volume constraint resolution.

Remark 3.7. (Boundary constraint). If $\Sigma(t) \cap \partial_e Z = \Gamma \neq \emptyset$ and $g(\cdot, \infty) = \lim_{t\to\infty} g(\cdot, t)$ is bounded, then the steady state solution ($V = 0$) to (1.1) corresponds to a surface $\Sigma(\infty)$ with prescribed mean curvature $\kappa = -g(\cdot, \infty)$ and given boundary Γ, and it can be computed as the asymptotic limit of $\Sigma(t)$ as $t \to \infty$. Since $a \ge a^* > 0$, the time step τ^i has always a lower bound proportional to $(ha^*)^2$. DMA can thus be used to approximate $\Sigma(\infty)$ with Σ^i as $i \to \infty$.

Remark 3.8 (Range of application). DMA extends naturally to higher dimensions, provided an efficient mesh generator is available, and it also couples naturally with (finite element) solvers for physical quantities in the bulk; these issues are being investigated. If a uniform partition of the entire domain Ω is used, as is done for LS, then the implementation of an active domain D^i would be rather simple. We show in Section 5.1.1, however, that this strategy can be drastically improved via a graded dynamic mesh. On the contrary, advecting a surface in 3D is a nontrivial procedure, particularly to past singularities, thereby making the use of FT restrictive.

4. DYNAMIC MESH ALGORITHM: IMPLEMENTATION

We now describe computational issues that dictate practicality and efficiency of DMA. Updating the mesh $\mathscr{D}^i$ and finite element matrices to follow the layer motion are far from being trivial tasks. If properly implemented, they result in savings of both computing time and memory allocation, and give more flexibility in selecting the local meshsize.

4.1. *Mesh Definition and Updating*

The algorithm actually computes mass and stiffness matrices $\mathbf{M}^i_1$, $\mathbf{M}^i_0$, $\mathbf{M}^i_{-1}$, and $\mathbf{K}^i$ for the dynamic mesh $\mathscr{D}^i$, updates τ^i on imposing (3.5), and finally solves (3.6) within D^i. We stress that $\mathscr{D}^i$ is minimal in terms of the number of triangles.

Once X^{i+1} and $T^{i+1} \subset D^i$ have been determined, $\mathscr{D}^i$ is updated as follows. First, all *security* triangles S of $\mathscr{D}^i$, namely $S \cap T^i \neq \emptyset$, S, that do not intersect T^{i+1} any more are removed because they are no longer needed. New triangles are next created at all nodes on the boundary of T^{i+1} that are not interior to D^i. The mesh so obtained is $\mathscr{D}^{i+1}$.

4.2. *Mesh Generation*

We resort to an advancing front algorithm in the spirit of [28]. In order to construct the first mesh, the moving mesh front (l) is set initially to be a partition of ∂Z, together with the boundary of an equilateral triangle in the interior of each connected component of the initial transition region $\mathscr{T}_\varepsilon(0)$, both graded according to $\mathscr{H}(\mathbf{z})$. Starting from the seed(s), the mesh generator adds new triangles of size comparable with $\mathscr{H}(\mathbf{z})$ for as long as nodes of l are found to belong to $\mathscr{T}_\varepsilon(0)$.

This dynamic mesh $\mathscr{D}^{i+1}$, consistent with $\mathscr{H}(\mathbf{z})$, is generated using the advancing front algorithm which allows us to either delete or incorporate efficiently an element to l. Since $\mathscr{D}^{i+1}$ cannot exit Z and must fit the grid on ∂Z, l comprises also $\partial Z \backslash \partial D^{i+1}$. In fact l is always the boundary of the subregion of Z not yet partitioned, but the nodes on $\partial Z \backslash \partial D^{i+1}$ are properly flagged, thereby ruling out any computation on them. The deletion of triangles is a new feature with respect to [28]. At this stage we either remove or add the corresponding contributions to the global matrices. It is worth noting that the insertion of new triangles can create new nodes, while the elimination of triangles can lead to removal of nodes. In these cases it is necessary to add or remove rows and columns of matrices. This is not accomplished by a complete renumbering of the nodes, which would be inefficient, but by marking rows/columns which have been removed, so that they can be used later when new nodes are added. This illustrates the strong linkage between mesh generation and matrix handling.

Even though $\mathscr{D}^i$ is weakly acute, such a property may fail to hold for $\mathscr{D}^{i+1}$. It is then necessary to postprocess $\mathscr{D}^{i+1}$ by simply switching the common edge of adjacent triangles whenever the sum of the opposite angles exceeds π. This process is known to converge after finite iterations and to lead to a weakly acute triangulation. However, mass and stiffness matrices must be modified accordingly. This process introduces interpolation errors on X^i which might accumulate. Numerical experiments show that this happens occasionally and is restricted to a few elements, and so its cumulative effect is not expected to degrade accuracy. However, this issue deserves further investigation.

4.3. *Volume Constraint*

To effectively compute μ^{i+1} in (3.9) and (3.10), we can use a secant-like method, as in [8]. Since τ^i is small, we perform only one secant step and use the ratio at the previous time step as follows:

$$\begin{aligned} \mu^{i+1} &= \mu^i - r^i F^{i+1}(\mu^i), \\ r^{i+1} &= \frac{\mu^{i+1} - \mu^i}{F^{i+1}(\mu^{i+1}) - F^{i+1}(\mu^i)}. \end{aligned} \tag{4.1}$$

Quantities in the denominator of r^{i+1} verify

$$F^{i+1}(\mu^i) = F^i(\mu^i) + \int_Z (X^i(\mu^i) - X^{i+1}(\mu^i))\,\zeta\,d\mathbf{z},$$

$$F^{i+1}(\mu^{i+1}) = F^i(\mu^i) + \int_Z (X^i(\mu^i) - X^{i+1}(\mu^{i+1}))\,\zeta\,d\mathbf{z}.$$

These corrections only involve solving (3.9) and thus dealing with the active domain D^i. The global cost of each time step of scheme (3.9) and (3.10) is just slightly higher than that of (3.6) because of the extra work involved in updating only the diagonal term $g^{i+1} = \mu^{i+1}$ in (3.6) with μ^{i+1} obtained from (4.1). At the beginning, an extra cost is required for computing r^0 which amounts to about one step of (3.6). Satisfaction of (3.10) can be verified a posteriori. FT could also be implemented efficiently to handle the global volume constraint in 2D (see [7]).

5. NUMERICAL SIMULATIONS

We present a number of numerical experiments carried out on a SUN Sparc II workstation for the geometric motion in 2, 3, 4, and 8 dimensions, with axial symmetries. Motion by mean curvature (plus forcing), volume constraint, and minimal surfaces are discussed. We employ the following notation:

ω^0: initial datum of (1.4);

$\Sigma^{0,\lambda} = \{\mathbf{z} \in Z : \omega^0(\mathbf{z}) = \lambda\}$: initial interface;

$I^{0,\lambda} = \{\mathbf{z} \in Z : \omega^0(\mathbf{z}) < \lambda\}$ = Inside $(\Sigma^{0,\lambda})$ if $\Sigma^{0,\lambda}$ is closed;

$d^{0,\lambda}$: signed distance function of $\Sigma^{0,\lambda}$ (negative in $I^{0,\lambda}$);

$X^0 = \sum_{j=1}^{J^0} \gamma(d^{0,\lambda}(\mathbf{z}_j)/\varepsilon a((\mathbf{z}_j + \mathbf{s}(\mathbf{z}_j))/2)\varphi_j$: initial datum of DMA;

$f = X^0$ on $\partial_e Z$: boundary datum;

$X(\cdot, t)$: computed solution at time t;

$|A_\varepsilon^\lambda(t)|$: volume (area) of set $A_\varepsilon^\lambda(t) = \{\mathbf{x} \in \Omega : X(\mathbf{x}, t) \le 0\}$ to detect fattening;

S^k, D^k: k-sphere and k-disk, as topological manifolds;

$a(\mathbf{z})$: density function ($\mathscr{E}(\mathbf{z}) = \varepsilon a(\mathbf{z})$: relaxation parameter, $\mathscr{H}(\mathbf{z}) = ha(\mathbf{z})$: meshsize);

$t_\dagger$: extinction time; $t_*, t_*^\lambda, t_{**}^\lambda$: critical times; t_m^λ: monotonicity change.

We indicate the topology of both $\Sigma^{0,\lambda}$ and $I^{0,\lambda}$ using S^k and D^k in such a way that, e.g., a torus of dimension $n = n_1 + n_2$ is written as $S^{n_1-1} \times S^{n_2} = \partial(S^{n_1-1} \times D^{n_2+1})$. The function $d^{0,\lambda}$ is given either in closed form or easily computed via a Newton procedure for the minimization of dist $(\cdot, \Sigma^{0,\lambda})$, based on a parametric representation of $\Sigma^{0,\lambda}$.

5.1. *Motion by Mean Curvature*

Let $g = 0$. We impose $f = 1$ on $\partial_e Z$ because $\Sigma^\lambda(t) \subset \Omega$ for all $t > 0$. Asymptotic accuracy and performance of DMA is fully documented for the case of a shrinking circle for which the exact solution is known.

TABLE I

Shrinking Circle of Initial Radius $\lambda = 1$ (Dynamic Mesh Algorithm, $a(\mathbf{z}) = \max(0.1, |\mathbf{z}|)$)

h	ε	J	I	CPU	E^t	E^d
.1414	.4149	136	2711	31	.0390	.1718
.1000	.3454	194	3831	66	.0284	.1360
.0707	.2810	278	7699	193	.0185	.0972
.0500	.2247	437	16326	644	.0119	.0678
.03536	.1773	683	23735	1656	.0070	.0432
.02500	.1383	995	49784	5244	.0031	.0202
.01768	.1070	1492	106581	16580	.0011	.0075
.01250	.0822	2210	196739	47354	.0003	.0022

5.1.1. *Circle.* $S^1 = \partial(D^2)$. Let $Z = [0, 2)^2$, $n_1 = n_2 = 1$ with reflection and

$$\omega^0(\mathbf{z}) = |\mathbf{z}|, \quad \lambda = 1.$$

The evolving circle $r(t) = \sqrt{1 - 2t}$ shrinks to a point at $t_\dagger = \frac{1}{2}$. Table I summarizes the experiments performed with DMA for $a(\mathbf{z}) = \max(0.1, |\mathbf{z}|)$ and $\varepsilon = 1.5h|\log h|$ and used the additional notation:

J: average number of spatial degrees of freedom;

I: number of time steps;

CPU: computing time in seconds;

E^t: $L^{\text{in}}(0, 0.49)$-error for the expected extinction time;

$E^d = \max_{t^i \in (0,0.49)} \text{dist}(\Sigma(t^i), \Sigma^i)$: Hausdorff distance between interfaces.

We compare the full mesh strategy (the whole mesh and matrices are generated once, but the computation of the solution and the stability constraint are performed only in the enlarged transition region) with DMA. The full mesh strategy, which obviously requires a bigger memory allocation but avoids mesh updating, is also more expensive in terms of CPU time than DMA (compare Tables I and II).

TABLE II

Shrinking Circle of Initial Radius $\lambda = 1$ (Full Mesh, $a(\mathbf{z}) = \max(0.1, |\mathbf{z}|)$)

h	ε	J	I	CPU	E^t	E^d
.1414	.4149	280	2581	43	.0414	.1792
.1000	.3454	524	4742	131	.0307	.1438
.0707	.2810	1026	7830	408	.0202	.1042
.0500	.2247	1978	13815	1347	.0125	.0705
.03536	.1773	3873	22623	4098	.0071	.0437
.02500	.1383	7639	44903	15483	.0038	.0244

TABLE III

Shrinking Circle of Initial Radius $\lambda = 1$ (Dynamic Mesh Algorithm, Uniform Mesh)

h	ε	J	I	CPU	E^t	E^d
.05000	.2247	329	2465	84	.0464	.3048
.03536	.1773	489	7193	327	.0321	.2533
.02500	.1383	752	10391	835	.0220	.2098
.01768	.1070	1134	29835	3391	.0148	.1719
.01250	.0822	1688	43312	8272	.0098	.1240
.00884	.0627	2638	85218	25887	.0047	.0387
.00625	.0476	3937	170435	78920	.0031	.0237

This means that the overhead necessary to handle the dynamic mesh and matrices is more than compensated by just dealing with the active set as opposed to the entire domain. Striking comparisons for resolution of the singularity with the case $a = 1$ over a quasi-uniform mesh are reported in Table III.

5.1.2. *Tori.* We consider the evolution of various tori in 3D and 4D, with $Z = [0, 3)^2$ and

$$\omega^0(\mathbf{z}) = ((z_1 - 1)^2 + (z_2 - c)^2)^{1/2} \quad (c = 0, 1), 0 < \lambda < 1.$$

Numerical experiments are intended to determine critical radii λ_*, along with times t_* of singularity formation, separating evolutions with strikingly distinct topology.

5.1.2.1. *Torus.* $S^1 \times S^1 = \partial(S^1 \times D^2)$. Let $n_1 = 2$, $n_2 = 1$ with reflection and $c = 0$.

There exists a critical radius λ_* such that for all $\lambda < \lambda_*$ the surface shrinks to $S^1 \subset \{z_2 = 0\}$ and then suddenly disappears at $t_\dagger^\lambda$ (Fig. 5.1a), whereas for $\lambda > \lambda_*$ the surface focuses at the origin at some time t_*^λ, when a singularity occurs, then changes its topology to S^2 and eventually disappears at $t_\dagger^\lambda$ (Fig. 5.1b). Our numerical experiments with $a(\mathbf{z}) = \max(0.05, 0.07z_1 + 0.07z_2^2)$ yield

$$h = 0.1, \quad \varepsilon = 0.28: 0.64931264519 < \lambda_* < 0.64931264520$$
$$h = 0.05, \varepsilon = 0.15: 0.64298575535 < \lambda_* < 0.64298575536.$$

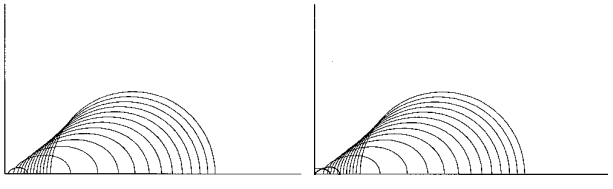

FIG. 5.1. Torus $S^1 \times S^1$, $n_1 = 2, n_2 = 1$ ($h = 0.05, \varepsilon = 0.15$), interfaces at $t = 0.025i$ and t_*^λ, t_m^λ (bold lines): (a) $\lambda = 0.64298575535$ ($t_m^\lambda = 0.296290$, $t_\dagger^\lambda = 0.298381$); (b) $\lambda = 0.64298575536$ ($t_*^\lambda = 0.295622$, $t_m^\lambda = 0.297845$, $t_\dagger^\lambda = 0.299720$).

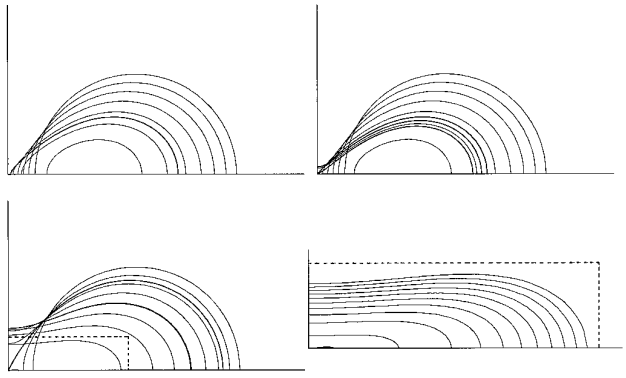

FIG. 5.2. Torus $S^1 \times S^2$, $n_1 = n_2 = (h = 0.05, \varepsilon = 0.15)$, interfaces at $t = 0.025i$ and $t_*^\lambda, t_{**}^\lambda, t_m^\lambda$ (bold lines): (a) $\lambda = 0.78556296$ ($t_m^\lambda = 0.111080$, $t_\dagger^\lambda = 0.170624$); (b) $\lambda = 0.78556298$ ($t_*^\lambda = 0.111617$, $t_m^\lambda = 0.119092$, $t_{**}^\lambda = 0.129542$, $t_\dagger^\lambda = 0.170844$); (c) $\lambda = 0.808$ ($t_*^\lambda = 0.040106$, $t_m^\lambda = 0.100950$, $t_{**}^\lambda = 0.198271$, $t_\dagger^\lambda = 0.198279$) and zoom (interfaces at $t = 0.0025i \geq 0.175$, and t_{**}^λ).

Uniqueness of the evolution has been proven together with the fact $t_\dagger^{\lambda *} = t_*^{\lambda *}$ [32].

5.1.2.2. *Torus.* $S^1 \times S^2 = \partial(S^1 \times D^3)$. Let $n_1 = n_2 = 2$ and $c = 0$.

The topology of $\Sigma^{0,\lambda}$ is so different from the previous one that leads to a quite distinct evolution. The numerical experiments with $a(\mathbf{z}) = \max(0.05, 0.07z_1 + 0.07z_2^2)$ show now the existence of two critical radii $0 < \lambda_* < \lambda_{**}$. For $\lambda < \lambda_*$ the surface shrinks at $t_\dagger^\lambda$ to $S^1 \subset \{z_2 = 0\}$ and suddenly disappears at $t_\dagger^\lambda$ (Fig. 5.2a). For $\lambda > \lambda_{**}$ a singularity develops at the origin at time t_*^λ, and then the surface becomes topologically equivalent to S^3 until it shrinks to the origin. For $\lambda_* < \lambda < \lambda_{**}$ the evolution is for a while similar to the case $\lambda > \lambda_{**}$, but a second singularity forms at the origin at a later time $t_{**}^\lambda > t_*^\lambda$ after which the surface becomes again a 4D-torus and shrinks at $t_\dagger^\lambda$ to $S^1 \subset \{z_2 = 0\}$ and disappears (Figs. 5.2c and d). Figure 5.2b corresponds to λ slightly bigger than λ_*, as revealed by $\Sigma^\lambda(t_*^\lambda)$ and $\Sigma^\lambda(t_{**}^\lambda)$ being very close to each other. Our simulations suggest:

$$\lim_{\lambda \downarrow \lambda_*} t_*^\lambda = \lim_{\lambda \downarrow \lambda_*} t_{**}^\lambda < \lim_{\lambda \downarrow \lambda_*} t_\dagger^\lambda, \quad \lim_{\lambda \uparrow \lambda_{**}} t_{**}^\lambda = \lim_{\lambda \uparrow \lambda_{**}} t_\dagger^\lambda.$$

This would imply that the evolution is unique for both critical values λ_* and λ_{**}. Moreover,

$$h = 0.1, \varepsilon = 0.28 : 0.78943557 < \lambda_* < 0.78943558,$$
$$0.7965 < \lambda_{**} 0.7970$$
$$h = 0.05, \varepsilon = 0.15 : 0.78556296 < \lambda_* < 0.78556298,$$
$$0.8090 < \lambda_{**} < 0.8092.$$

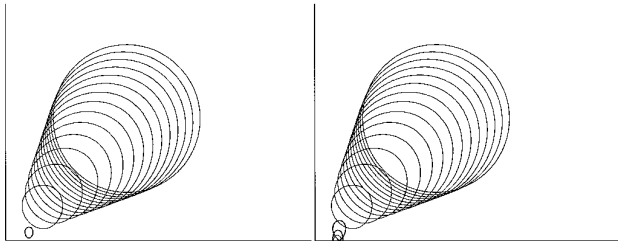

FIG. 5.3. Torus $S^1 \times S^1 \times S^1$, $n_1 = n_2 = 2$ ($h = 0.05$, $\varepsilon = 0.15$), interfaces at $t = 0.025i$ and t^λ_*, t^λ_m (bold lines): (a) $\lambda = 0.6049754$ ($t^\lambda_m = 0.348538$, $t^\lambda_\dagger = 0.349333$); (b) $\lambda = 0.6049755$ ($t^\lambda_* = 0.347062$, $t^\lambda_m = 0.349223$, $t^\lambda_\dagger = 0.350379$).

A recent result by Ilmanen *et al.* [2] would suggest that the surface at time t^λ_{**} is tangent to a 4D-cone at the origin with opening $\approx\pi/4$ which develops fattening. Detecting fattening (nonuniqueness) for λ_* is a delicate issue which thus deserves further numerical investigation. We note that the proposed density function is not adapted to select λ_{**} with high accuracy, because of the large curvature of the front near the z_1-axis at times $t \approx t^\lambda_*$.

5.1.2.3. *Torus.* $S^1 \times S^1 \times S^1 = \partial(S^1 \times S^1 \times D^2)$. Let $n_1 = n_2 = 2$ and $c = 1$.

A critical radius λ_* separates smooth evolutions until extinction time $t^\lambda_\dagger$, case $\lambda < \lambda_*$, from singularity formation at symmetric positions on the axes at time $t^\lambda_* < t^\lambda_\dagger$, namely the S^1 manifolds $(z^\lambda_*, 0)$, $(0, z^\lambda_*)$. Our experiments with $a(\mathbf{z}) = \max(0.05, \min(z_1, z_2))$ suggest that (see Figs. 5.3a, b)

$$\lim_{\lambda \downarrow \lambda_*} z^\lambda_* = 0, \quad \lim_{\lambda \downarrow \lambda_*} t^\lambda_* = \lim_{\lambda \downarrow \lambda_*} t^\lambda_\dagger,$$

which means that for $\lambda = \lambda_*$ the surface shrinks to a point without change of topology (no fattening!). Moreover, we have the following approximate λ_*:

$$h = 0.1, \quad \varepsilon = 0.28 : 0.6202511 < \lambda_* < 0.6202512$$
$$h = 0.05, \varepsilon = 0.15 : 0.6049754 < \lambda_* < 0.6049755.$$

It is apparent that mesh asymmetry influences the evolution, as shown in Figs. 5.3a, b. Mesh evolution is shown in Figs. 5.4a–f for $\lambda = 0.625$, $h = 0.1$, $\varepsilon = 0.28$, and various time steps. The evolving front, as well as the triangulation, are connected before the onset of singularities, as illustrated in Figs. 5.4a–c. At t^λ_* and after, both front and mesh split into two connected components (see Fig. 5.4d). This situation remains until the interior front disappears along with the corresponding mesh, at t^λ_{**}. Then there are only one front and mesh left, as depicted in Figs. 5.4e–f. Topological mesh changes are handled automatically by DMA.

5.2. *Fattening:* $2S^1 = \partial(2D^2)$

We simulate the evolution of two circles which may be nonunique for suitable critical radii after a critical time t_* (see [4]). To detect fattening we resort to Remark 2.2 and stress the occurrence of a large jump in $|A^\lambda_\varepsilon|$ with just a change in the sixth decimal digit of λ. We impose $f = 1$ on $\partial_e Z$ because $\Sigma^\lambda(t) \subset \Omega$ for $0 < t < T$ with $T > t_*$.

5.2.1. *Fattening with* $g = g(t)$. Let $Z = [0, 5)^2$, $n_1 = n_2 = 1$ with reflection and

$$\omega^0(\mathbf{z}) = |\mathbf{z} - (c, 0)| - 1, \quad g(t) = t - 2,$$

with $c > 0$ to be chosen. The initial interface $\Sigma^{0,\lambda}$ is composed of two disjoint circles of radius $1 + \lambda$ for $-1 <$

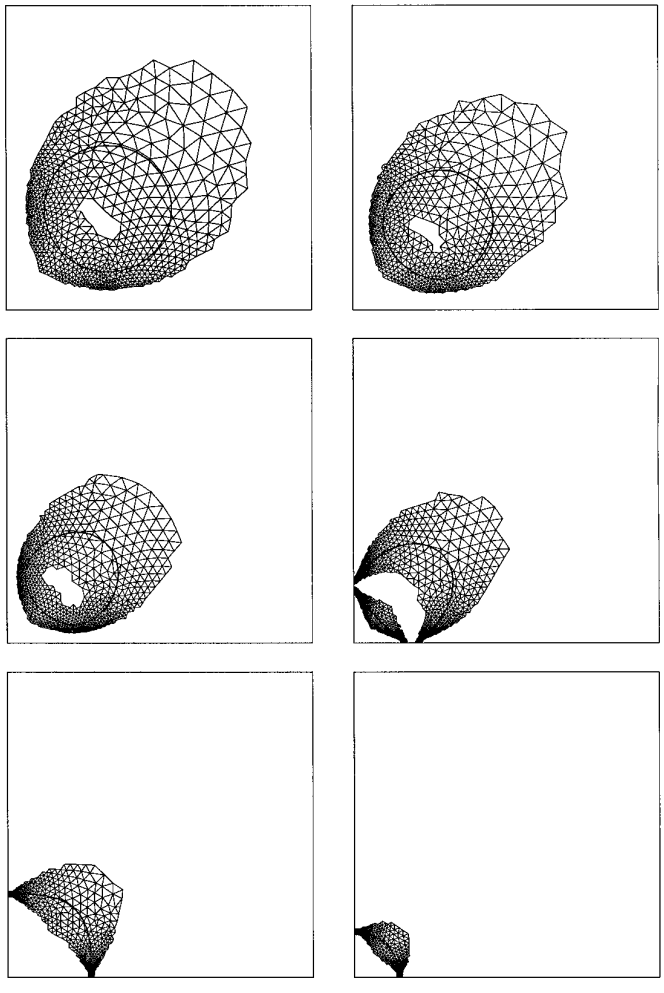

FIG. 5.4. Torus $S^1 \times S^1 \times S^1$, $n_1 = n_2 = 2$, $\lambda = 0.625$ ($a(\mathbf{z}) = \max(0.05, \min(z_1, z_2))$, $h = 0.1$, $\varepsilon = 0.28$): mesh and interfaces at $t = 0.1i \le t^\lambda_\dagger = 0.432997$ and $t^\lambda_* = 0.235113$.

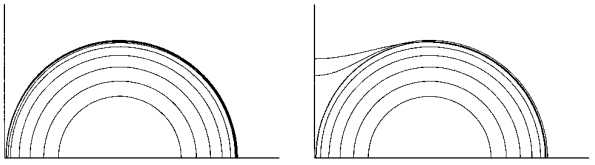

FIG. 5.5. Fattening $2S^1$, $g(t) = t - 2$ ($h = 0.1$, $\varepsilon = 0.28$), interfaces at $t = 0.25i \le 1.75$ and t_m^λ, t_*^λ (bold lines): (a) $\lambda = 0.0089$ ($t_m^\lambda = 1.312928$); (b) $\lambda = 0.0090$ ($t_*^\lambda = 1.258503$, exact $t_*^\lambda = 1.288830$).

$\lambda < c - 1$. For $0 < t < t_\dagger^\lambda$, let $r^\lambda(t)$ be defined by the ODE

$$r'(t) + \frac{1}{r(t)} + g(t) = 0, \quad r^\lambda(0) = 1 + \lambda.$$

For $\lambda = 0$ there exists $t_*^0 > 0$, where $r^0(t)$ attains a strict maximum $r^0(t_*^0)$ [4]. We then set $c = r^0(t_*^0)$. The evolution $\Sigma^\lambda(t)$ of $\Sigma^{0,\lambda}$ is symmetric with respect to the coordinate axes for all λ. For $\lambda < 0$, $\Sigma^\lambda(t)$ is regular and consists of two circles of radius $r^\lambda(t)$ centered at $(\pm c, 0)$. For $\lambda > 0$, instead, $\Sigma^\lambda(t)$ consists of two circles of radius $r^\lambda(t)$ for $t < t_*^\lambda = \min\{t > 0 : r^\lambda(t) \ge c\}$, whereas $\Sigma^\lambda(t)$ develops a singularity at the origin for $t = t_*^\lambda$. We note that $\Sigma^\lambda(t)$ changes its topology for $t > t_*^\lambda$ and the exact solution is no longer known and that fattening takes place at t_*^0 for $\lambda = 0$. The critical time t_*^0 and the center $c = r^0(t_*^0)$ can be computed easily with a simple ODE solver:

$$t_*^0 \approx 1.471847, \quad c \approx 1.893391.$$

The purpose of our numerical simulation is to study the behavior of $\Sigma^\lambda(t)$ around $\lambda = 0$. This is depicted in Fig. 5.5, which was obtained with

$$a(\mathbf{z}) = \max(0.05, 1 - \exp(-\tfrac{2}{3}z_1 - \tfrac{4}{9}z_2^2)),$$
$$h = 0.1,$$
$$\varepsilon = 0.28.$$

The computed area of the region $A_\varepsilon^\lambda(1.75)$ for $-0.1 \le \lambda \le 0.1$ is shown in Fig. 5.6, where it is compared with the exact area $2\pi(r^\lambda(1.75))^2$ of two circles that evolve independently (dotted line). The notorious jump in $|A_\varepsilon^\lambda|$ corresponds to the numerical critical values $\lambda = 0.0089, 0.0120, 0.0127$ and represents evidence of fattening.

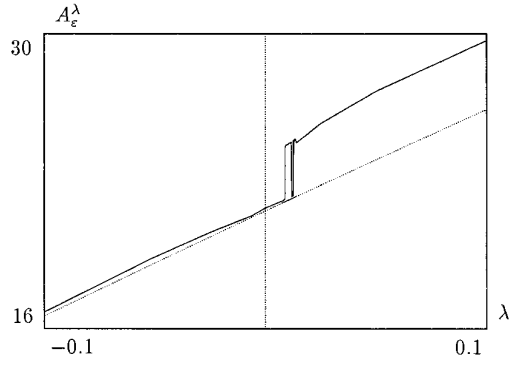

FIG. 5.6. Fattening $2S^1$, $g(t) = t - 2$ ($h = 0.1$, $\varepsilon = 0.28$); area of $A_\varepsilon^\lambda(1.75)$ and $2\pi(r^\lambda)^2(1.75)$ (dotted line) for $-0.1 \le \lambda \le 0.1$.

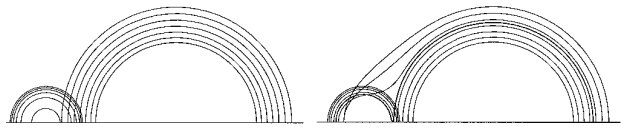

FIG. 5.7. Fattening $2S^1$, $g = -1$ ($h = 0.15$, $\varepsilon = 0.41$), interfaces at $t = 0.25i \le 1.5$ and t_*^λ (bold lines): (a) $\lambda = -0.00570$; (b) $\lambda = -0.00565$ ($t_*^\lambda = 0.882864$, $c + r^\lambda(t_*^\lambda) = C - R^\lambda(t_*^\lambda) = 0.0975$, exact $c + r^\lambda(t_*^\lambda) = 0.067752$, exact $C - R^\lambda(t_*^\lambda) = 0.118293$).

5.2.2. *Fattening with constant forcing.* Let $Z = (-7, 7) \times [0, 7)$ and $n_1 = n_2 = 1$ without reflection around the x_2-axis; hence $z_1 = x_1$, $z_2 = |x_2|$. Let

$$\omega^0(\mathbf{z}) = \min\left(\frac{1}{0.9}|\mathbf{z} - (c, 0)|, \frac{1}{2}|\mathbf{z} - (C, 0)|\right) - 1, \quad g = -1,$$

with $c < 0 < C$ to be chosen. Then $\Sigma^{0,\lambda}$ is given by two disjoint circles of radii $0.9(1 + \lambda)$ and $2(1 + \lambda)$ for $-1 < \lambda < (C - c)/2.9 - 1$. For $0 < t < t_\dagger^\lambda$, let the radii $r^\lambda(t)$ and $R^\lambda(t)$ be the solutions of the ODEs

$$r'(t) + \frac{1}{r(t)} = 1, \quad r^\lambda(0) = 0.9(1 + \lambda), \quad R^\lambda(0) = 2(1 + \lambda).$$

For $\lambda = 0$ there exists $t_*^0 > 0$, where $r^0(t) + R^0(t)$ attains a strict maximum [4]. Hence, letting $c = -r^0(t_*^0)$ and $C = R^0(t_*^0)$, for $\lambda < 0$ the evolution $\Sigma^\lambda(t)$ of $\Sigma^{0,\lambda}$ is regular up to the extinction time $t_\dagger^\lambda$ of the small circle: the small circle shrinks to a point and the big circle expands according to $r^\lambda(t)$ and $R^\lambda(t)$. For $\lambda > 0$ a singularity develops at $(C - R^\lambda(t_*^\lambda), 0) = (c + r^\lambda(t_*^\lambda), 0)$ at $t_*^\lambda = \min\{t > 0 : r^\lambda(t) + R^\lambda(t) \ge C - c\}$. For $\lambda = 0$ the interface $\Sigma^\lambda(t)$ fattens up at time t_*^0. The critical time t_*^0 and the centers $c = -r^0(t_*^0)$ and $C = R^0(t_*^0)$ can be computed upon solving numerically the corresponding ODEs:

$$t_*^0 \approx 1.055741, \quad c \approx -0.619546, \quad C \approx 2.591233.$$

The numerical simulation is carried out with (see Fig. 5.7)

$$a(\mathbf{z}) = \max(0.05, 1 - \exp(-\tfrac{2}{3}((x - 0.05)_+ + 0.9(x)_- - \tfrac{4}{9}z_2^2)), \quad h = 0.15, \varepsilon = 0.41.$$

The computed area of the region $A_\varepsilon^\lambda(1.5)$ for $-0.1 \le \lambda \le$

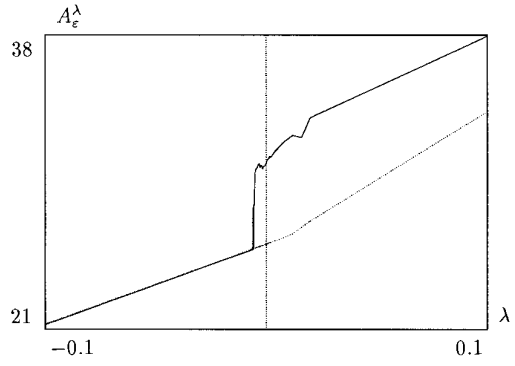

FIG. 5.8. Fattening $2S^1$, $g = -1$ ($h = 0.15$, $\varepsilon = 0.41$): area of $A_\varepsilon^\lambda(1.5)$ and $\pi((r^\lambda)^2(1.5) + (R^\lambda)^2(1.5))$ (dotted line) for $-0.1 \le \lambda \le 0.1$.

0.1 is shown in Fig. 5.8 and is compared with the exact area $\pi((r^\lambda)^2(1.5) + (R^\lambda)^2(1.5))$ of two circles evolving independently (dotted line). The abrupt change of slope of the dotted curve takes place at the value $\lambda \approx 0.011337$ for which the small circle disappears at $t = 1.5$. Note the jump in $|A_\varepsilon^\lambda|$ corresponding to the numerical critical values $\lambda = -0.00565, -0.00585$.

5.3. *Minimal Surfaces*

We approximate minimal surfaces or surfaces with constant mean curvature $\Sigma(\infty)$ with given boundary Γ by seeking the asymptotic limit of $\Sigma(t)$ as $t \to \infty$ (see Remark 3.7).

5.3.1. *Cathenoid.* Let $Z = \{|\mathbf{z}| < 1\}$, $n_1 = 1$ with reflection and $n_2 = 2$; hence, $\partial_e Z = \{|\mathbf{z}| = 1\}$. Given $P = (\cos \alpha, \sin \alpha)$ for $0 < \alpha < \pi/2$, we seek minimal surfaces $\Sigma(\infty)$ in Z with boundary P, which consists of two circles S^1. To this end we impose $\Gamma = \Sigma(t) \cap \partial_e Z = \{P\}$ and the initial interface to be $\Sigma^{0,\lambda} = P\overline{P} \cap Z$, where $\overline{P} = (\lambda, 0)$ for $|\lambda| < 1$. The simulations are depicted in Fig. 5.9 and were done, with

$$\alpha = \frac{\pi}{3} > \alpha_*, \quad \lambda = -0.1, 0,$$

$$a(\mathbf{z}) = 1 \text{ (quasi-uniform mesh } \mathscr{D}^i), \quad h = 0.01, \quad \varepsilon = 0.035.$$

Here $\alpha_* = \arctan(\cosh(c_*)/c_*) \approx 0.985515$, where $c_* \tanh c_* = 1$ is the critical angle such that for $\alpha_* < \alpha < \pi/2$ there exists two values $k_1 < k_2$ and corresponding cathenoids $\Sigma^i_{**} = \{z_2/k_i = \cosh(z_1/k_i)\} \ni P$ $(S^1 \times D^1)$ with Σ^2_{**} minimal and Σ^1_{**} stationary; Σ^2_{**} is the asymptotic limit of $\Sigma(t)$ in Fig. 5.9.a. If $\alpha = \alpha_*$ then $k_1 = k_2$ and Σ^1_{**} is stationary. The surface $\Sigma_* = \{z_1 = \cos \alpha\}$ $(2D^2)$ is minimal for all α and is the asymptotic limit in Fig. 5.9.b.

5.3.2. *Curve with constant curvature.* Let Z be either $Z = [0, L)^2$ or $Z = [0, L)^2 \backslash [L - l, L)^2$, and $n_1 = n_2 = 1$ with reflection, along with

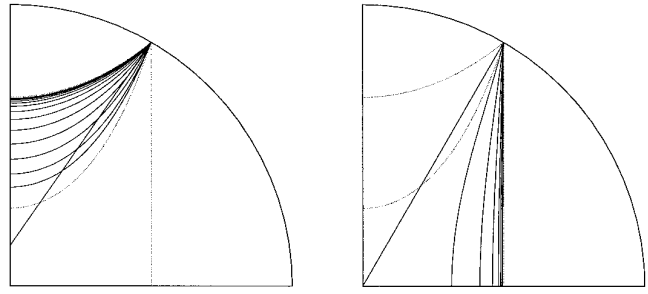

FIG. 5.9. Cathenoid, $\alpha = \pi/3$, $k_1 = 0.276495$, $k_2 = 0.670934$ ($h = 0.01$, $\varepsilon = 0.035$), Σ_*, Σ^1_{**}, Σ^2_{**} (dotted lines) and interfaces at $t = 0.1i \le T$: (a) $\lambda = -0.1$ ($T = 1.5$); (b) $\lambda = 0$ ($T = 1$).

$$\omega^0(\mathbf{z}) = |\mathbf{z}|, \quad f = 1, g = -k.$$

We seek a curve $\Sigma_* = \partial(I_*)$ with constant curvature $k > 0$ in Z and tangential contact at $\partial_e Z$, where I_* is any set contained in $\overline{Z}$ that minimizes the functional $\mathscr{F}(I) = |\partial I \cap (0, \infty)^2| - \int_I k$ [5, 6]. The empty set is always a relative minimum of $\mathscr{F}$. The other minima of $\mathscr{F}$ correspond to sets with boundary Σ_* composed of circular arcs of radius $1/k$ intersecting tangentially with $\partial_e Z$, or normally with the reflection axes, or passing through the reentrant corner $(L - l, L - l)$ with angles less or equal than $\pi/4$.

The initial curve $\Sigma^{0,\lambda}$ is a circle of radius $0 < \lambda < \min(L, \sqrt{2}(L - l))$. If $k\lambda > 1$, then $\Sigma^\lambda(t)$ grows towards Σ_*, with I_* being either a relative or absolute minimum of $\mathscr{F}$. Simulations performed with $a(\mathbf{z}) = \max(0.1, 1 - \exp(-\text{dist}(\mathbf{z}, \partial_e Z))$ and $h = 0.1$, $\varepsilon = 0.28$ are depicted in Fig. 5.10 for both cases with and without reentrant corner. A boundary layer is always present because of the Dirichlet condition $f = 1$ necessary to enforce zero contact angle at $\partial_e Z$. This layer consists of very few triangles. If $k\lambda = 1$, then $\Sigma^\lambda(t) = \Sigma^{0,\lambda}$ correspond to a stationary (not minimal) point of $\mathscr{F}$. If $k\lambda < 1$, instead, then $\Sigma^\lambda(t)$ shrinks in finite time to the origin.

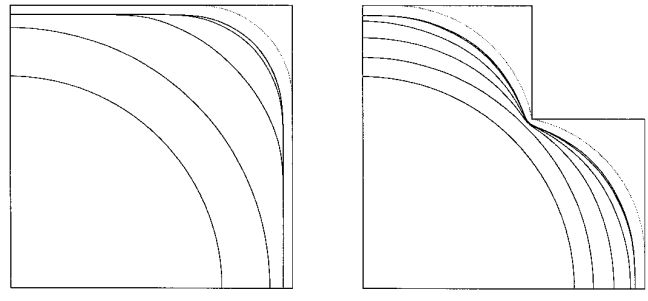

FIG. 5.10. Curve with constant curvature k and tangential contact at the boundary ($h = 0.1$, $\varepsilon = 0.28$), exact solutions (dotted lines) and interfaces at $t = 0.1i \le 0.5$, $L = 1$, $\lambda = 0.75$: (a) $l = 0$, $k = 3$; (b) $l = 0.4$, $k = 2$.

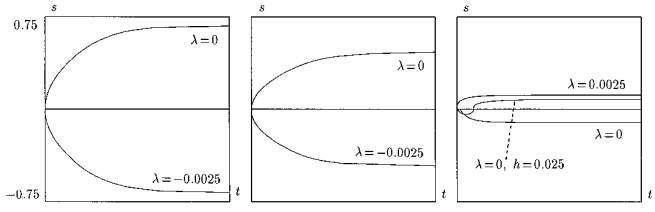

FIG. 5.11. Cones ($h = 0.05$, $\varepsilon = 0.15$), profile of $s = z_1 - z_2$ for $\Sigma^i \cap (\{z_1 = 0\} \cup \{z_2 = 0\})$: (a) $n_1 = n_2 = 1$, $\lambda = 0$, and $\lambda = -0.0025$; (b) $n_1 = n_2 = 2$, $\lambda = 0$, and $\lambda = -0.0025$; (c) $n_1 = n_2 = 4$, $\lambda = 0$, and $\lambda = 0.0025$, $\lambda = 0$ for $h = 0.025$, $\varepsilon = 0.08$.

5.3.3. *Cones.* We examine and compare the following three cases with $Z = \{|\mathbf{z}| < 1\}$, $\partial_e Z = \{|\mathbf{z}| = 1\}$, $g = 0$, and $\omega^0(\mathbf{z}) = z^1 - z_2$:

(a) $n_1 = n_2 = 1$ with reflection,

(b) $n_1 = n_2 = 2$,

(c) $n_1 = n_2 = 4$.

The initial surface $\Sigma^{0,\lambda}$ exhibits a nonunique evolution (fattening) for $\lambda = 0$ and cases (a), (b). Case (c) corresponds to the minimal cone of Simons, which was studied in [9] and requires at least dimension 8 of the ambient space. The discrete evolution for $\lambda = 0$ is thus dictated by mesh asymmetries. To capture fattening we compute evolutions for values of λ around 0 and use Remark 2.2. The cancellation taking place in (2.3) and the large value of the principal curvatures for $\lambda \neq 0$ small, together, make these tests difficult for FT.

The simulations were carried out with $a(\mathbf{z}) = \max(0.05, |\mathbf{z}|)$ and $h = 0.05$, $\varepsilon = 0.15$. The graphs of $s = z_1 - z_2$ versus time for the intersection of Σ^i with the coordinate axes are depicted in Figs. 5.11a–c for all three cases. It is apparent that the initial velocity is infinite and the deviation from stationarity is much more pronounced in cases (a), (b). This effect is further substantiated in Fig. 5.11c for case (c) with $\lambda = 0$, $h = 0.025$, and $\varepsilon = 0.08$: the front moves initially very slowly to the top, but then it stops and recedes. Fattening is shown in Fig. 5.12, where the area of $A^\lambda_\varepsilon(0.1)$ is plotted versus λ for $|\lambda| \leq 0.1$. In striking contrast to cases (a) and (b), Simons cone, case (c), appears

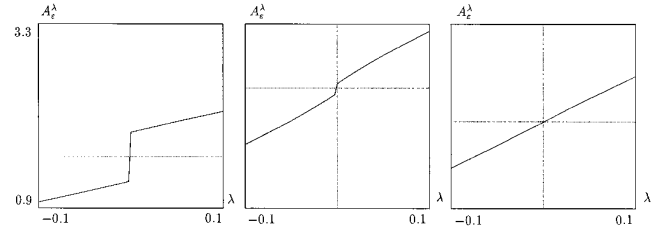

FIG. 5.12. Cones ($h = 0.05$, $\varepsilon = 0.15$), area of $A^\lambda_\varepsilon(0.1)$ for $-0.1 \leq \lambda \leq 0.1$: (a) $n_1 = n_2 = 1$; (b) $n_1 = n_2 = 2$; (c) $n_1 = n_2 = 4$.

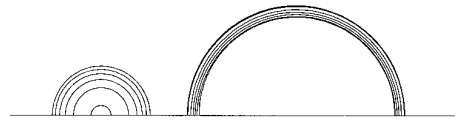

FIG. 5.13. Two circles ($2S^1$) under volume constraint, $\lambda = 0$ ($h = 0.1$, $\varepsilon = 0.28$); interfaces at $t = 0.05i \leq 0.5$; $|A^\lambda_\varepsilon(0.5)| = 3.892855$, $|I^{0,\lambda}| = 3.926991$.

to be numerically "stable," even in the presence of mesh asymmetries and diffusion ($\varepsilon > 0$).

5.4. *Volume Preserving Mean Curvature Flow*

We present examples, with $f = 1$ because $\Sigma(t) \subset \Omega$ for all $t > 0$, of curvature driven evolution with volume constraint. It is important to realize that LS does not apply, whereas DMA does extend rather easily (see Remark 4.3).

5.4.1. *Circles.* $2S^1$. Let $Z = (-4, 4) \times [0, 4)$ with $n_1 = n_2 = 1$ and no reflection around the x_2-axis; thus $z_1 = x_1$, $z_2 = |x_2|$. Since

$$\omega^0(\mathbf{z}) = \min(2|\mathbf{z} - (-1, 0)|, |\mathbf{z} - (1, 0)|) - 1,$$

$\Sigma^{0,\lambda}$ consists of two disjoint circles of radii $\frac{1}{2}(1 + \lambda)$ and $1 + \lambda$ for $-1 < \lambda < \frac{1}{3}$. We employ the volume constraint $|A^\lambda(t)| = |I^{0,\lambda}|$. The smaller circle shrinks to a point at time $t^\lambda_\dagger$ and the larger one grows, both maintaining their shape; their radius are $r(t)$ and $R(t)$. The evolution thus remains regular up to $t^\lambda_\dagger$ and is stationary thereafter. A simulation with $a(\mathbf{z}) = \max(0.05, 1 - \exp(-\min(|\mathbf{z} - (-1, 0)|, |\mathbf{z} - (1, 0)|)))$, $h = 0.1$, $\varepsilon = 0.28$, and $\lambda = 0$ is shown in Fig. 5.13. A rapid variation of the Lagrange multiplier μ^{i+1} takes place near $t^\lambda_\dagger$. This is related to the behavior of the nonlocal forcing term $g = (1/|\Sigma^\lambda(t)|) \int_{\Sigma^\lambda(t)} \kappa$ which jumps from $2/R(t^\lambda_\dagger)$ to $1/R(t^\lambda_\dagger)$ across time $t^\lambda_\dagger$. The secant method of Section 4.3 does not fail even at this stage, as the agreement between $|A^\lambda_\varepsilon(t)|$ and $|I^{0,\lambda}|$ reveals.

5.4.2. *Circloids.* $2S^1$. Let $Z = [0, 3)^2$ and $n_1 = n_2 = 1$ with reflection, together with

$$\omega^0(\mathbf{z}) = 2|\mathbf{z} - (1, 1)| - 1 \quad \text{if } z_2 \geq 1,$$
$$\omega^0(\mathbf{z}) = 2|1 - z_1| - 1 \quad \text{if } z_2 < 1.$$

Therefore $\Sigma^{0,\lambda}$ is made of two disjoint circloids for $|\lambda| < 1$. The inside $I^{0,\lambda}$ of $\Sigma^{0,\lambda}$ is the union of a rectangle of height 1 and base $1 + \lambda$ with a semicircle on top of radius $\frac{1}{2}(1 + \lambda)$ and center $(1, 1)$. Since we enforce symmetry across the axes, the evolution subject to $|A^\lambda(t)| = |I^{0,\lambda}|$ only develops a singularity at time t^λ_* when $|I^{0,\lambda}| > 2\pi$, that is, $\lambda > \lambda_* \approx 0.097655$. Thus, for $\lambda < \lambda_*$, DMA will find an approximation of the metastable solution consisting of two identical circles. For $\lambda > \lambda_*$, instead, the surface $\Sigma(\infty)$ is a circle

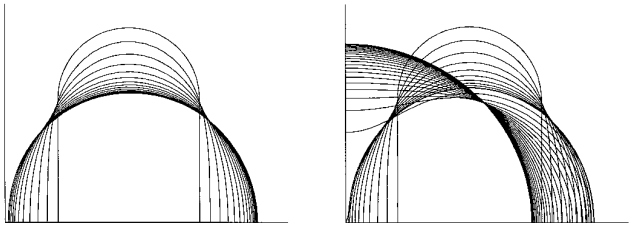

FIG. 5.14. Two circloids ($2S^1$) under volume constraint ($h = 0.1$, $\varepsilon = 0.28$); interfaces at $t = 0.1i \leq T$ and t^λ_* (bold line): (a) $\lambda = 0.14$, $T = 1.5$, $|A^\lambda_\varepsilon(T)| = 6.615729$, $|I^{0,\lambda}| = 6.601407$; (b) $\lambda = 0.16$, $T = 3$, $|A^\lambda_\varepsilon(T)| = 6.798959$, $|I^{0,\lambda}| = 6.753664$.

centered at the origin, and $t^\lambda_* \to \infty$ as $\lambda \downarrow \lambda_*$. Two simulations with $\lambda = 0.14$ and $\lambda = 0.16$, obtained with $a(\mathbf{z}) = \max(0.05, 1 - \exp(-\frac{2}{3} z_1 - \frac{4}{9} z_2^2))$ and $h = 0.1$, $\varepsilon = 0.28$, are drawn in Fig. 5.14. They corroborate the above comments and exhibit a good agreement between $|A^\lambda_\varepsilon(t)|$ and $|I^{0,\lambda}|$. Note that the critical parameter λ_* is not selected with high accuracy because the evolution is halted at a relatively small time $T = 1.5$, and simulations use a rather large value of h and ε.

6. CONCLUSIONS

We have shown how to exploit key features of a double obstacle formulation of a singularly perturbed reaction-diffusion PDE in devising DMA, a competitive method for the geometric motion of fronts. Crucial properties of DMA are:

(a) *Insensitivity to singularity formation.* Topological changes are handled automatically, requiring no user intervention nor a priori classification of singularities.

(b) *Local structure.* A rather thin (discrete) noncoincidence or active set is present at a given instant, thereby leading to a computational complexity typical of $\mathbb{R}^{n-1}$ and much better than LS, which increases the space dimension by one. See Section 5.1.1.

(c) *Range of application.* Our approach extends naturally to higher dimensions, requiring only an efficient mesh generator, whereas implementing FT in 3D is a difficult task.

(d) *Enhanced resolution.* A space-dependent relaxation parameter allows variable layer thickness. This can be effectively used near singularities not only to resolve them but also to ensure accuracy of the discrete flow past singularities. See Section 5.1.2.3.

(e) *Convergence.* The method is proven to converge past singularities without any assumptions on the flow (1.1) [21–26, 29]. This renders the present results more reliable in comparison to FT and LS, which are not known to converge.

(f) *Critical cases.* Most simulations examine singularities for which the principal curvatures blow up but their sum remains comparatively small. New singularities for tori seem to emerge. See Sections 5.1.2, 5.3.3.

(g) *Volume constraint.* This can be easily accommodated via a Lagrange multiplier and needs no significant computational effort. In contrast, LS does not apply.

(h) *Discretization.* DMA uses piecewise linear finite elements, with mass lumping, over a dynamic mesh for space discretization and forward differences in time, with adaptive control of the time step. Explicit time-stepping guarantees that at most one layer of elements has to be added or deleted per time step, thereby making mesh updating simple and, thus, practical. Stability constraints are dictated by the smallest meshsize within the active set. Small time steps much thus be enforced only when singularities develop, whereas relatively large time steps are allowed at the beginning or past singularities, when the evolution is smooth. This compares favorably with LS which uses uniform meshes and severe stability constraints throughout the entire calculation. No iteration is involved not even to meet the obstacle constraints.

(i) *Potentials*. DMA exhibits desirable computational properties and potentials that make it appropriate as a building block for adaptive solvers of complex phase transitions. The adaptive design of a space-time dependent relaxation parameter is being studied, along with a 3D version of DMA. They both are prerequisites for coupling DMA with other evolution laws for the bulk.

REFERENCES

1. D. Adalsteinsson and J. A. Sethian, preprint, 1993.
2. S. Angenent, T. Ilmanen, and J. Velasquez, in preparation.
3. G. Barles, H.-M. Soner, and P. E. Souganidis, *SIAM J. Control Optim.* **31,** 439 (1993).
4. G. Bellettini and M. Paolini, *Atti Accad. Naz. Lincei Cl. Sci. Fis. Mat. Natur. Rend.* (*9*) *Mat. Appl.* **5,** 229 (1994).
5. G. Bellettini, M. Paolini, and C. Verdi, *Atti Accad. Naz. Lincei Cl. Sci. Fis. Mat. Natur. Rend.* (*9*) *Mat. Appl.* **1,** 317 (1990).
6. G. Bellettini, M. Paolini, and C. Verdi, *Calcolo* **27,** 251 (1991).
7. G. Bellettini, M. Paolini, and C. Verdi, "Front-Tracking and Variational Methods to Approximate Interfaces with Prescribed Mean Curvature," in *Proc. Numerical Methods for Free Boundary Problems,* (P. Neittaanmäki, Ed.) (Birkhäuser, Basel, 1991), p. 83.
8. J. F. Blowey and C. M. Elliott, "Curvature Dependent Phase Boundary Motion and Parabolic Double Obstacle Problems, in *IMA Vol. Math. Appl.*, 47 edited by J. L. Vazquez *et al.* (Springer-Verlag, New York, 1993), 19.
9. E. Bombieri, E. De Giorgi, and E. Giusti, *Invent. Math.* **7,** 243 (1969).
10. K. A. Brakke, *The Motion of a Surface by its Mean Curvature* (Princeton Univ. Press, Princeton, NJ, 1978).
11. L. Bronsard and R. V. Kohn, *J. Differential Equations* **90,** 211 (1991).
12. L. Bronsard and B. Stoth, CMU Research Report No. 94-NA-008, 1994.

13. J. W. Cahn, C. A. Handwerker, and J. E. Taylor, *Acta Metall.* **40,** 1443 (1992).
14. Y. G. Chen, Y. Giga, and S. Goto, *J. Differential Geom.* **33,** 749 (1991).
15. P. G. Ciarlet, *The Finite Element Method for Elliptic Problems* (North-Holland, Amsterdam, 1978).
16. G. Dziuk, *Numer. Math.* **58,** 603 (1991).
17. L. C. Evans, H.-M. Soner, and P. E. Souganidis, *Commun. Pure Appl. Math.* **45,** 1097 (1992).
18. L. C. Evans and J. Spruck, *J. Differential Geom.* **33,** 635 (1991).
19. T. Ilmanen, *J. Differential Geom.* **38,** 417 (1993).
20. R. H. Nochetto, M. Paolini, S. Rovida, and C. Verdi, ''Variational Approximation of the Geometric Motion of Fronts,'' in *Motion by Mean Curvature and Related Topics,* edited by G. Buttazzo and A. Visintin (Gruyter, Berlin, 1994), p. 124.
21. R. H. Nochetto, M. Paolini, and C. Verdi, *Math. Models Methods Appl. Sci.* **3,** 771 (1993).
22. R. H. Nochetto, M. Paolini, C. Verdi, *Ann. Scuola Norm. Sup. Pisa Cl. Sci.* (*4*) **21,** 193 (1994).
23. R. H. Nochetto, M. Paolini, C. Verdi, *Asymptotic Anal.* **10,** 173 (1995).
24. R. H. Nochetto and C. Verdi, *SIAM J. Math. Anal.*, to appear.
25. R. H. Nochetto and C. Verdi, *SIAM J. Numer. Anal.*, to appear.
26. R. H. Nochetto and C. Verdi, *Numer. Math.*, to appear.
27. S. Osher and J. A. Sethian, *J. Comput. Phys.* **79,** 12 (1988).
28. M. Paolini and C. Verdi, *Riv. Inform.* **20,** 251 (1990).
29. M. Paolini and C. Verdi, *Asymptotic Anal.* **5,** 553 (1992).
30. J. Rubinstein and P. Sternberg, *IMA J. Appl. Math.* **48,** 249 (1992).
31. J. A. Sethian, *J. Differential Geom.* **31,** 131 (1990).
32. H.-M. Soner and P. E. Souganidis, *Commun. Partial Differential Equations* **18,** 859 (1993).
33. O. C. Zienkiewicz, *The Finite Element Method in Engineering Science* (McGraw–Hill, London, 1971).